ORIGINAL PAPER

CrossMark

Dynamic Mechanical Properties and Fracturing Behavior of Marble Specimens Containing Single and Double Flaws in SHPB Tests

Diyuan Li[1] · Zhenyu Han[1] · Xiaolei Sun[1] · Tao Zhou[2] · Xibing Li[1]

Abstract

Dynamic impact tests were conducted on rectangular marble specimens with flaws to investigate the effect of the flaw angles and ligament angles on the rock dynamic mechanical properties, fracturing behavior, and energy evolution characteristics. A 75-mm diameter split Hopkinson pressure bar (SHPB) device was used in the tests. The experimental results show that the flaw geometries have a strong effect on the dynamic mechanical properties and fracturing behavior of rocks. In general, the effects of the flaw angle and flaw number on the dynamic strength are more significant than the effect of the ligament angle. A high-speed camera was used to monitor and record the crack initiation and coalescence and the failure processes of the marble specimens in real-time. The crack propagation can be divided into two major stages, i.e., the formation of white patches and the generation of macrocracks. The white patches usually appear prior to the peak stress of the specimen. The shear cracks usually initiate at or near the flaw tips and propagate to form X or half-X shear belts that dominate the macroscopic failure under impact loading. Nine types of crack coalescence behaviors are identified for the marble specimens with double flaws, and the macro failure modes of the specimens is usually combined by some of them. The energy absorption properties of the marble specimen are also significantly affected by the pre-existing flaws. The energy absorption ratio can be maximized by setting a certain number of pre-existing flaws with an appropriate inclination angle and a proper ligament angle to effectively improve the fragmentation efficiency of rocks.

Keywords Rock dynamics · Flaw · Marble · Mechanical properties · Crack coalescence · Energy

List of Symbols

SHPB	Split-Hopkinson pressure bar
ISRM	International Society for Rock Mechanics
$2a$	Flaw length
α	Flaw inclination angle
$2b$	Ligament length
β	Ligament angle
$\varepsilon_I(t)$	Incident strain pulse
$\varepsilon_R(t)$	Reflected strain pulse
$\varepsilon_t(t)$	Transmitted strain pulse
$\sigma(t)$	Axial dynamic stress
$\varepsilon(t)$	Strain
$\dot{\varepsilon}(t)$	Strain rate
A_e	Cross-sectional area of the elastic bar
C_e	P-wave velocity of the elastic bar
E_e	Young's modulus of the elastic bar
A_s	Cross-sectional area of the specimen
L_s	Length of the specimen
HSC	High-speed camera
fps	Frames per second
σ_d	Dynamic compressive strength
ε_d	Axial strain corresponding to the peak stress
UCS	Uniaxial compressive strength
E_I	Incident energy
E_R	Reflected energy
E_T	Transmitted energy
$\rho_e C_e$	Wave impedance of the elastic bar
R	Ratio of absorbed energy to incident energy

✉ Diyuan Li
diyuan.li@csu.edu.cn

1 School of Resources and Safety Engineering, Central South University, Changsha 410083, Hunan, China

2 Department of Civil and Environmental Engineering, The Hong Kong Polytechnic University, Hung Hom, Hong Kong, China

1 Introduction

During the rock formation process and geological-tectonic evolution, a large number of defects such as cracks, voids, inclusions, weak planes, and joint sets are generated within the rock mass. The existence of these pre-existing natural defects poses potential threats to the stability and safety of structures built on/in the rock mass. Therefore, understanding the influences of the pre-existing defects on the rock mechanical and fracture behaviors is of great significance to the stability and safety assessment of rock structures.

In the past decades, great efforts have been devoted to studying the effects of pre-existing defects on the mechanical and fracture properties of rock and rock-like materials. Due to the heterogeneity of rock material, it is very difficult to investigate the rock failure mechanism using the classical fracture mechanics (Fang and Harrison 2002; Liang et al. 2012). Thereby, laboratory experiments, a fundamental method, have been widely used to study the mechanical and fracture behaviors of rocks under various loading conditions. For instance, the group at MIT led by Einstein systematically investigated the strength and fracturing of rock and rock-like (i.e., gypsum) materials containing pre-existing flaws under static compressions (Shen et al. 1995; Bobet and Einstein 1998; Li et al. 2005b; Wong and Einstein 2009a, b, c; Morgan et al. 2013), where the term ''flaw'' refers to an artificial crack. The geometries of the pre-existing flaws (e.g., inclination angle, ligament angle, flaw length, and arrangements of the flaws) have great impacts on the strength, deformation, and crack propagation and coalescence of the rock under static loading. Wong and Chau (1998) investigated the crack coalescence and strength of a sandstone-like material containing two parallel inclined frictional cracks under uniaxial compression. Three main modes of crack coalescence were observed: shear mode, mixed shear/tensile mode, and wing tensile mode. Yang et al. (2017) and Li et al. (2017a) studied the influence of pre-existing oval flaws on the deformational and fracture behaviors of natural rocks under static uniaxial compression. It was found that the compressive strength and Young's modulus were greatly weakened by the pre-existing oval flaws and the major principal stress and failure modes were dependent on the geometries of the oval flaws.

Aside from static loading conditions, dynamic loadings, e.g., earthquakes, blasts, and rockbursts, are also widespread in mining and geotechnical engineering. Under dynamic loading, it is recognized that the strength (i.e., the compressive, tensile, and shear strengths) of the rock is rate-dependent (Li et al. 2005a; Dai et al. 2010; Zhang and Zhao 2014). That is to say, the rock strength shows a remarkable increase with the increase in the loading rate (Li et al. 2017b). In the case of dynamic loading conditions, the propagation of the stress wave, the development of the deformation, and the migration of the fracture zone all occur at a higher speed than under static loading. A rock specimen with pre-existing flaws may exhibit different cracking behavior under dynamic loading than under static loading. For example, the numerical manifold method (NMM) has been used to investigate the stress wave propagation through fractured rocks and to model the dynamic fracture problems in rocks (Fan et al. 2013; Wu et al. 2013). To study the influence of dynamic loading on crack propagation, Zou and Wong (2014) and Li et al. (2017b) carried out laboratory tests using a split Hopkinson pressure bar (SHPB) on prismatic marble specimens containing a single pre-existing flaw with different inclination angles. Li et al. (2015) investigated the effects of a single pre-existing hole (circular and elliptical holes) on the fracture behaviors of marble specimens in SHPB tests. The authors found that shear cracks appeared earlier than tensile wing cracks and dominated the fracturing process under dynamic loading conditions. The failure mode of the flawed specimens under dynamic compression included the occurrence of an "X" shape regardless of the flaw inclination angle. Zhou et al. (2018) conducted dynamic tests on the behavior of cracks emanating from tunnel edges and demonstrated that the crack speeds were not constant and the propagation toughness was related to the crack speeds. The bearing capacity and failure patterns of the rock–shotcrete interface in underground engineering are sensitive to the strain rate and depth of the sawteeth of the interface (Luo et al. 2017). Additionally, a digital image correlation (DIC) technique was also used to measure the full-field strain of the rock surface to show the brittle failure micromechanisms prior to the occurrence of macroscopic cracks under dynamic loadings (Zhang and Zhao 2013).

Although the fracturing behavior of rocks has attracted growing concern, few studies have been conducted on the crack coalescence in the ligament area. The fact that the crack propagation and coalescence depend on the arrangement of the flaws is of great importance for the rock fracturing process because this process affects the strength and integrity of brittle materials (Morgan et al. 2013). Jiang et al. (2016) investigated the dynamic crack coalescence using a gypsum-like 3D printing material. Li et al. (2018) found that the stress perpendicular to the propagating crack and two-hole spacing both influenced the arresting cracks under blasting loads. In 1991 at a quarry in Hong Kong, a large block of rock slid from a steep rock face. The investigation report indicated that this event was induced by pre-existing joints that resulted from the blasting vibration (Wong and Chau 1998). Therefore, a study of the cracking and

coalescence behavior is of significant importance for the analysis of the failure mechanism of rock masses and can provide insights into the efficient breaking of rocks with artificial flaws under dynamic loading.

In view of this, SHPB tests were performed on prismatic marble specimens containing single and double pre-existing flaws to investigate the effects of the flaw geometries (i.e., flaw inclination angle, flaw number, ligament angle) on the dynamic mechanical properties, energy dissipation, and the dynamic crack propagation and coalescence of the marble specimens.

2 Experimental Methodology

2.1 Specimen Preparation

The rock material is a white marble with coarse grain particles composed of quartz (53%), calcite (44%), carbonaceous material (2%), and opaque minerals (1%) as determined by a mineral composition analysis and optical microscopy analysis (Fig. 1). The rock material has a crystalline structure with an average unit weight of approximately 2795 kg/m^3 and a uniaxial compressive strength (UCS) of 117.27 MPa. Following the method suggested by the International Society for Rock Mechanics (ISRM)

(Zhou et al. 2011), the ratio of length to width of the tested specimens is set at 1.0 with a nominal size of $60 \times 60 \times 30$ mm^3. The ends of the specimens were grinded and polished to unevenness and non-perpendicularity to less than 0.02 mm. The flaw geometry is described in Fig. 2, where $2a$ is the flaw length of 10 mm (a is half the length of the flaw), α is the flaw inclination angle (the angle between the flaw and loading direction), $2b$ is the ligament length (the distance between the inner tips of the two pre-existing flaws) of 20 mm, and β is ligament angle (the angle between the ligament and loading direction).

The pre-existing flaws were produced by a high-pressure water cutting method, which has been proven to cause no disturbance and damage to the other parts of the specimen (Li et al. 2017b). The opening of the flaw is about 1–1.5 mm. To investigate the effects of the geometries of the pre-existing flaws on the mechanical and fracture behaviors of the marble specimens under dynamic loading, three flaw parameters, i.e., flaw number, flaw angle, and ligament angle were taken into consideration. The detailed description of the marble specimens with different flaw geometries is listed in Table 1. The specimen number describes the type of rock, number of flaws, flaw inclination angle, and ligament angle. For example, M-1-30 refers to a single-flaw marble specimen with $\alpha = 30°$; M-2-45-30 denotes a marble specimen with double flaws with $\alpha = 45°$ and $\beta = 30°$.

Fig. 1 Photographs of marble obtained by thin section analysis; **a** single polarized light; **b** orthogonally polarized light
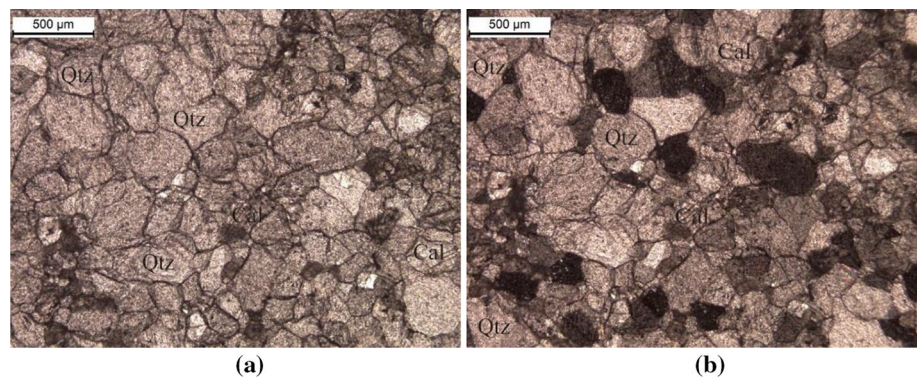

Fig. 2 Geometries of marble specimens. **a** A single-flawed specimen (α is the flaw inclination angle and $2a$ is the flaw length); **b** A specimen with double flaws (β is the ligament angle and $2b$ is the ligament length)
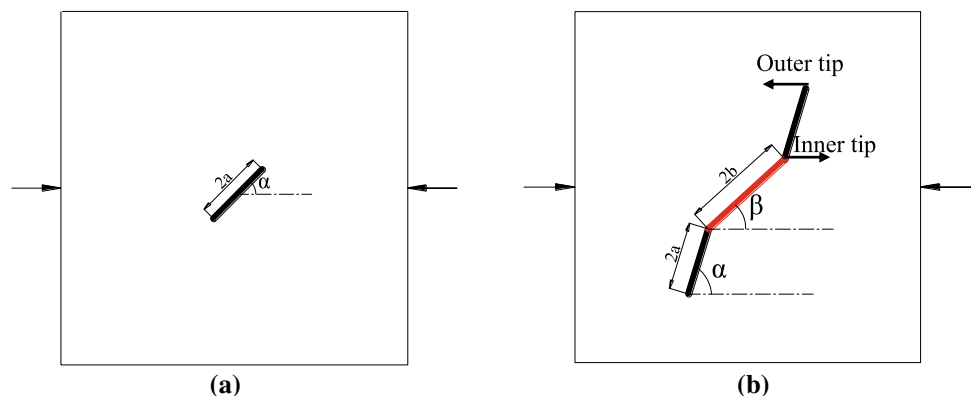
Table 1 Mechanical properties of intact and flawed specimens under SHPB tests

Specimen no.	L/mm	W/mm	H/mm	Flaw			σ_d/MPa	$\varepsilon_d/10^{-2}$	$\dot{\varepsilon}$/s^{-1}	Remark
				L_F/mm	α/°	β/°				
M$_0$	59.63	59.81	30.18	–	–	–	255	0.64	60.00	Intact specimen
M-1-0	60.92	60.71	30.88	10	0	–	229	0.31	65.43	Flaw angle
M-1-30	59.77	60.02	28.56	10	30	–	203	0.50	50.63	
M-1-45	59.51	59.74	28.49	10	45	–	210	0.50	57.20	
M-1-60	59.15	59.54	28.37	10	60	–	207	0.48	51.83	
M-1-75	59.48	59.31	28.52	10	75	–	205	0.47	51.33	
M-1-90	59.03	59.31	28.67	10	90	–	199	0.47	49.05	
M-2-0-30	59.66	59.86	29.68	10	0	30	210	0.53	46.80	Flaw angle
M-2-0-45	60.44	60.66	30.04	10	0	45	214	0.96	51.03	and ligament
M-2-0-75	60.28	60.47	31.67	10	0	75	208	0.94	53.40	angle
M-2-30-30	59.46	59.54	28.40	10	30	30	193	0.58	63.80	
M-2-30-45	59.92	59.96	28.41	10	30	45	199	0.55	55.90	
M-2-30-75	59.33	59.65	28.55	10	30	75	187	0.52	47.67	
M-2-45-30	60.33	60.77	30.09	10	45	30	187	0.59	61.56	
M-2-45-45	60.40	59.52	29.30	10	45	45	190	0.56	66.8	
M-2-45-75	60.36	60.81	30.69	10	45	75	166	0.56	49.13	
M-2-60-30	60.30	60.30	30.58	10	60	30	164	0.96	56.35	
M-2-60-45	60.49	61.01	30.88	10	60	45	170	0.89	50.80	
M-2-60-75	60.74	60.92	30.48	10	60	75	165	0.84	59.77	
M-2-75-30	60.34	60.72	30.95	10	75	30	153	0.94	76.45	
M-2-75-45	60.38	60.55	30.35	10	75	45	161	0.93	61.93	
M-2-75-75	60.67	60.88	30.69	10	75	75	154	0.87	70.00	
M-2-90-30	60.76	60.70	30.82	10	90	30	139	0.99	70.25	
M-2-90-45	60.16	60.48	31.53	10	90	45	167	1.05	69.53	
M-2-90-75	60.38	60.49	30.44	10	90	75	152	1.00	75.25	

2.2 Testing Equipment

The laboratory tests were carried out on a modified SHPB device, which consists of a gas gun, a cone-shaped striker (0.54 m in length), an incident bar and a transmitted bar (2 m in length), an absorbing bar (0.8 m in length), and a data acquisition device (Li et al. 2005a, 2009; Zhou et al. 2011; Zhang and Zhao 2014; Li 2014; Xia and Yao 2015). The diameter, P-wave velocity, elastic modulus, and density of the three bars are 75 mm, 5400 m/s, 240 GPa, and 7810 kg/m^3, respectively.

During testing, the specimen is sandwiched between the incident and transmitted bars with some lubricant on the surfaces of the specimen and bars. The impact of the cone-shaped striker on the front surface of the incident bar produces a slowly rising half-sine wave (Li et al. 2005a; Qiu et al. 2017). When the compressive wave (incident wave) reaches the bar-specimen interface, a portion is reflected into the incident bar (reflected wave) and another portion is transmitted through the specimen and then enters the transmitted bar (transmitted wave). These three elastic stress pulses are recorded (as shown in Fig. 3) by the strain gauges mounted on the bars and are denoted as the incident strain pulse $\varepsilon_I(t)$,
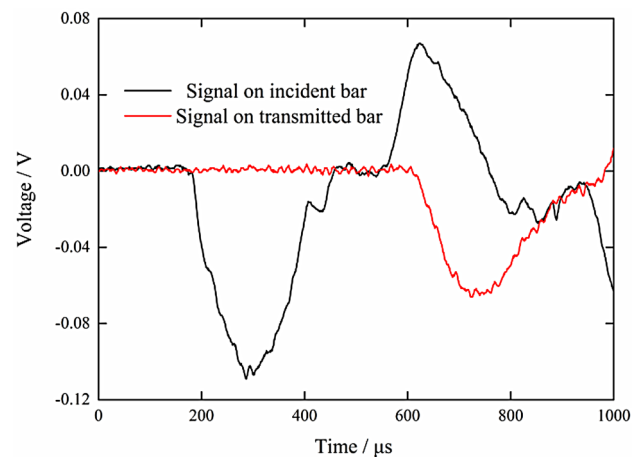

Fig. 3 Electrical signals captured from the strain gauges (specimen M-1-30)

reflected strain pulse $\varepsilon_R(t)$, and transmitted strain pulse $\varepsilon_t(t)$, respectively. According to the one-wave propagation theory,

the axial stress $\sigma(t)$, strain $\varepsilon(t)$, and strain rate $\dot{\varepsilon}(t)$ are derived by the following equations (Li 2014):

$$\sigma(t) = \frac{A_e E_e}{2A_s}[\varepsilon_I(t) + \varepsilon_R(t) + \varepsilon_T(t)] \tag{1}$$

$$\varepsilon(t) = \frac{C_e}{L_s}\int_0^t [\varepsilon_I(t) - \varepsilon_R(t) - \varepsilon_T(t)]\,\mathrm{d}t \tag{2}$$

$$\dot{\varepsilon}(t) = \frac{C_e}{L_s}[\varepsilon_I(t) - \varepsilon_R(t) - \varepsilon_T(t)], \tag{3}$$

where A_e, C_e, and E_e are the cross-sectional area, P-wave velocity, and Young's modulus of the elastic bar, respectively. A_s and L_s are the cross-sectional area and length of the specimen, respectively.

In SHPB tests, the loading and failure processes are usually completed within hundreds of microseconds. To observe and analyze the fracture behaviors of the flawed marble specimens, a SA1.1 high-speed camera (HSC) was used to monitor and record the real-time fracturing process. The HSC was set at a frame rate of 80,000 fps (frames per second) with a resolution of 256×176 pixels. During testing, the HSC was triggered by a transistor–transistor logic pulse generated by an oscilloscope synchronously with the incident signal.

3 Experimental Results and Discussion

3.1 Stress Equilibrium

In SHPB tests, it is essential to achieve a stress equilibrium between the ends of the specimen prior to the failure,
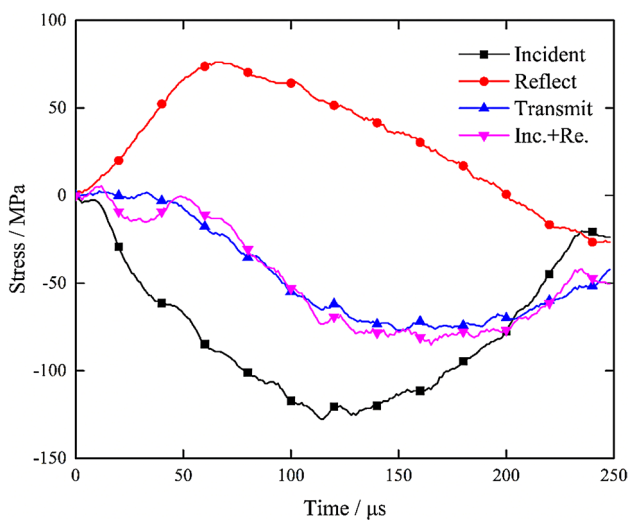
Fig. 4 Dynamic stress equilibrium in specimen M-1-30

particularly prior to the peak stress in the specimen. In this study, a cone-shaped striker was used to generate a slowly rising half sine wave to achieve a constant strain rate loading and dynamic stress equilibrium at the ends of the specimen (Zhou et al. 2011; Li 2014; Li et al. 2017b). Figure 4 shows the dynamic stress equilibrium for the specimen M-1-30. The sum of the incident stress and reflected stress is almost equal to the transmitted stress in the vicinity of the peak stress. This demonstrates that the stress equilibrium can be achieved and maintained for the marble specimens with pre-existing flaws and the result is thus valid for the present SHPB tests (Qiu et al. 2017).

3.2 Dynamic Stress–Strain Curves

The complete dynamic stress–strain curves of the intact and flawed marble specimens are plotted in Fig. 5. It is evident that the flaw geometries have significant effects on the dynamic stress–strain curves of the marble specimens.

The dynamic stress–strain curves of the flawed marble specimens can be approximately divided into three stages: (1) the linear elastic deformation stage (OA or section I in Fig. 5e), where the stress increases linearly with increasing strain; (2) the crack initiation and growth stage (AB or section II in Fig. 5e), during which stress concentration is produced at or near the tips of the pre-existing flaws, thereby initiating and propagating cracks during the loading process (Inglis 1913; Jeong et al. 2005; Wang et al. 2014; Li et al. 2016); (3) the macroscopic failure during the final stage (BC or section III in Fig. 5e). For example, it is observed in Fig. 5e that, for the single-flaw specimens, the stress–strain curves have a long linear elastic deformation stage (OA) and a shorter plastic stage (AB). Subsequently, the curves drop rapidly (BC) and brittle failure occurs. For the specimens with double flaws, the duration of the linear elastic deformation stage (section I) is shorter but the platform (section II) around the peak stress is longer. Then the curves descend slowly in the post-peak region (section III), which may be caused by the crack coalescence in the ligament area and far-field crack propagation. These results indicate that the increase in the number of flaws results in more ductile of the rock specimens.

3.3 Dynamic Strength

The dynamic strength and strain at the peak stress of the flawed specimens are listed in Table 1, where σ_d is the dynamic compressive strength and ε_d is the axial strain corresponding to the peak stress. Figures 6 and 7 show the effects of the number of flaws, inclination angle, and ligament angle on the dynamic strength and strain of the flawed marble specimens in the SHPB tests, respectively. It is clear
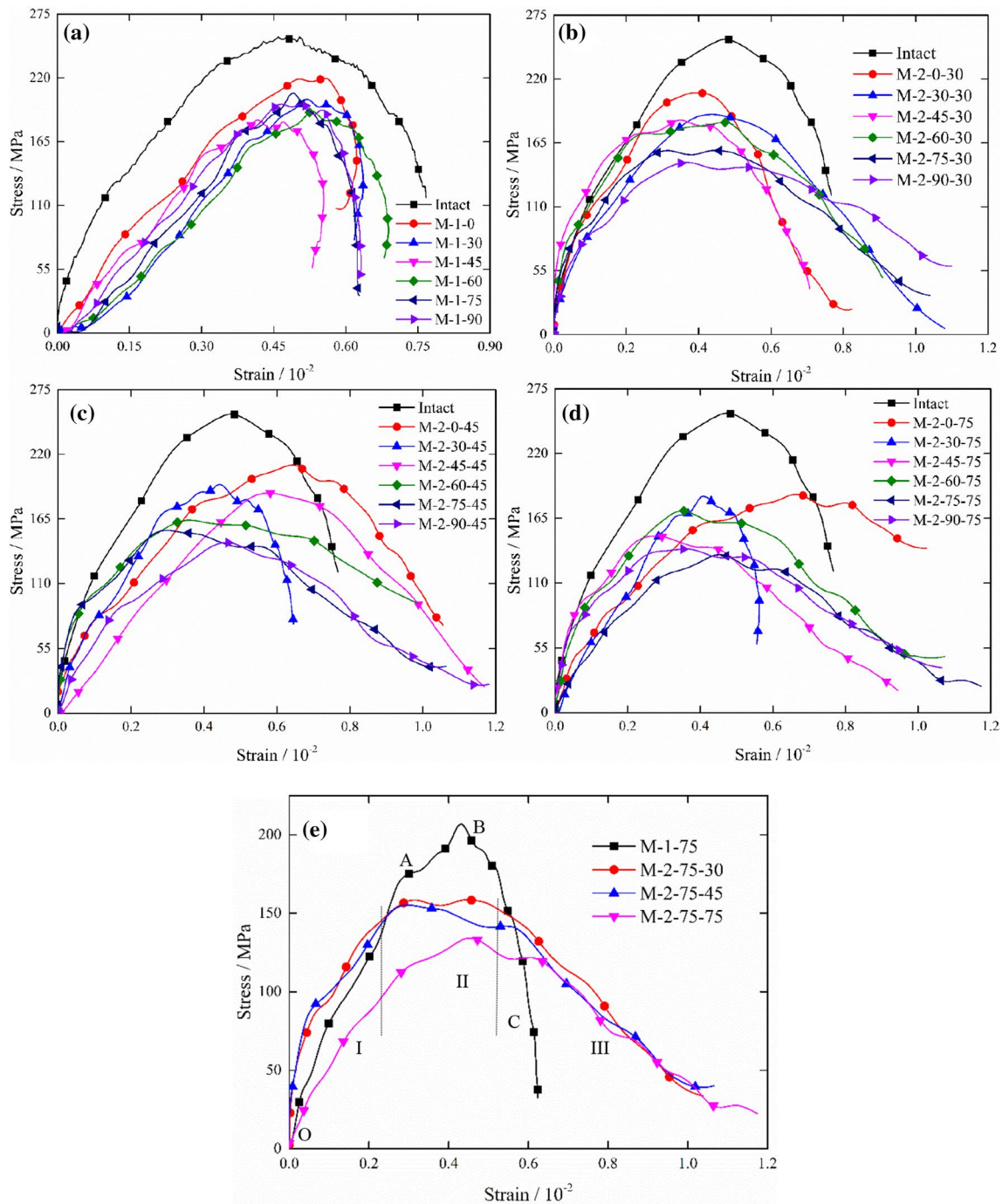
Fig. 5 Dynamic stress–strain curves of intact and flawed specimens. **a** specimens with a single pre-existing flaw; **b** specimens with double pre-existing flaws of $\beta = 30°$; **c** specimens with double pre-existing flaws of $\beta = 45°$; **d** specimens with double pre-existing flaws of $\beta = 75°$; **e** dynamic stress–strain curves of flawed specimens with flaw angle of 75° (OA, AB, BC are for specimen with a single flaw; I, II, III are for specimens with double flaws)

that the flaw geometry has a strong effect on the dynamic mechanical properties of the marble specimens.

As shown in Fig. 6, the dynamic strength is lower for the flawed specimens than for the intact specimen (255 MPa for M_0). For the single-flaw specimens, the dynamic strength gradually decreases as the flaw angle increases from 0° to 90°. The specimen with an angle of 90° has the lowest strength (199 MPa) and exhibits a reduction in strength of about 22% compared with the intact specimen. In addition, it can be seen from Fig. 6
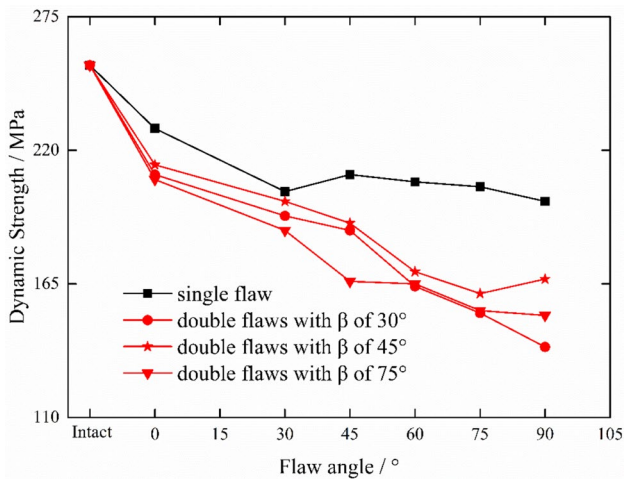
Fig. 6 Influence of flaw number, flaw angle and ligament angle on the dynamic strength of marble specimens under SHPB tests
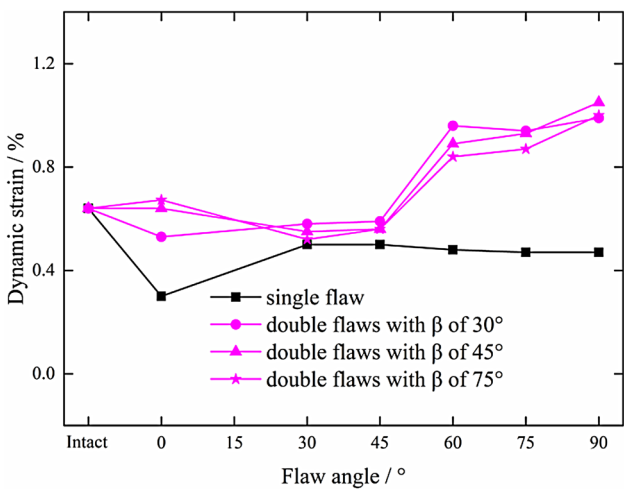

Fig. 7 Influence of flaw number, flaw angle and ligament angle on the deformation of marble specimens under SHPB tests

that the dynamic strength decreases dramatically when $\alpha < 30°$ but it changes marginally when $30° < \alpha < 90°$. For specimens with double flaws, the dynamic strength is affected not only by the flaw inclination angle α, but also by the ligament angle β. The dynamic strength gradually decreases as the flaw inclination angle increases from 0° to 90°. As shown in Fig. 6, for the double-flaw specimen with the same flaw angle, the dynamic strength reaches the maximum value when the ligament angle $\beta = 45°$ and the minimum value usually occurs at the ligament angle $\beta = 75°$, except for the specimen with a flaw angle of 90°. The results in Fig. 6 also show that the flaw number affects the strength of the flawed specimens. The strength of the specimens with double flaws is apparently lower than that

of the specimens with a single pre-existing flaw for the same flaw angle.

Based on these results, it can be concluded that the dynamic strength is closely related to the flaw geometries. The rock strength is greatly weakened by flaws with a larger α and an appropriate β. The effects of the flaw angle and flaw number on the dynamic strength are more significant than the effect of the ligament angle.

3.4 Dynamic Strain

Figure 7 shows the effects of the flaw geometry on the dynamic strain at the peak stress. The dynamic strain ε_d of the intact specimen is 0.64%. The dynamic strain is lower for the single-flaw specimens than the intact specimen with reductions ranging from 21.88 to 51.56%. The value decreases dramatically when $\alpha = 0°$ but changes marginally when α is between 30° and 90°. However, the dynamic strains are larger for the specimens with double flaws than for the intact specimen, except when α is 30° or 45° and it increases dramatically when α is larger than 30°. The influence of the ligament angle is less remarkable than that of the flaw angle for specimens with double flaws, which is illustrated in Fig. 7. The results in Fig. 7 also show that the flaw number affects the strain of the flawed specimens. The strains are larger for the specimens with double flaws than the specimens with a single flaw and the difference increases when the flaw angle is greater than 30°.

Based on these results, it can be concluded that the dynamic deformation is dependent on the flaw geometries (i.e., flaw angle, flaw number, and ligament angle). The effects of the flaw angle and flaw number on the dynamic deformation are greater than the effects of the ligament angle.

3.5 Comparison of Mechanical Properties under Quasi-static and Dynamic Loadings

Yang et al. (2009) have devoted considerable research effort to investigate the effect of double-flaw geometry on the strength and deformation behavior of marble specimens under uniaxial compression. A comparison of their research results with our present experimental results indicates that the strain rate has a significant influence on the mechanical properties and failure behaviors of marble specimens with double flaws.

It should be noted that only two ligament angles were used in Yang's tests (Yang et al. 2009) but three ligament angles were used in our tests. Therefore, we only discuss the influence of the flaw angle on the static and dynamic mechanical properties of the marble specimens. Table 2 summarizes the strength and peak strain of the marble

Table 2 Mechanical properties of marble specimens with double flaws under static and dynamic loadings

Flaw angle/°	Strength / MPa				Strain / 10^{-2}			
	Static results (Yang et al. 2009)	Dynamic results			Static results (Yang et al. 2009)	Dynamic results		
		$\beta=30°$	$\beta=45°$	$\beta=75°$		$\beta=30°$	$\beta=45°$	$\beta=75°$
30	57.08	193	199	187	0.271	0.58	0.55	0.52
45	50.66	187	190	166	0.263	0.59	0.56	0.56
60	35.88	164	170	165	0.111	0.96	0.89	0.84

specimens with double flaws under static and dynamic loadings. The results show that the compressive strength decreases with the increase in the flaw angle in both the static and dynamic tests. The static peak strain has a distinctly nonlinear inverse relationship with the increasing flaw angle. However, the dynamic peak strain increases with the increase in the flaw angle under dynamic loading, particularly when α is equal to 60°.

4 Fracture Behaviors

4.1 White Patches

White patches that are generated prior to the initiation of the macrocracks in marble specimens have been reported in many studies (Wong and Einstein 2009a, b, c; Lee and Jeon 2011; Zhang and Zhao 2013; Yin et al. 2014; Li et al. 2017b). Wong and Einstein (2009a, b, c) systematically investigated the evolution mechanism of the white patches in marble and gypsum specimens by microscopic [scanning electron microscopy (SEM)] and macroscopic observations and claimed that the macrocracks initiate and propagate along the white patch trajectories.

Two types of white patches, i.e., shear and tensile white patches, were observed in this research. The names of the white patches are based on the characteristics of the macrocracks that subsequently developed in the trajectory of the white patches. For instance, if a tensile crack generates along the trajectory of a white patch, the white patch is called a tensile white patch (Li et al. 2017b). Shear white patches mainly extend along the diagonal directions at an angle to the loading direction of the specimen and always generate an X or half X-shaped fracture filled with pulverized rock powder. However, tensile white patches usually develop smoothly in a curvilinear or linear path almost collinear to the loading direction. Table 3 shows the evolution of the white patches in a specimen with double flaws under dynamic loading, taking the specimen M-2-2-45 as an example. Shear white patches emanate
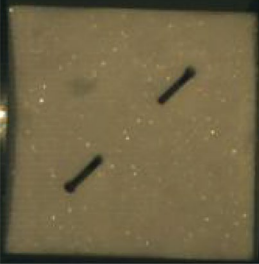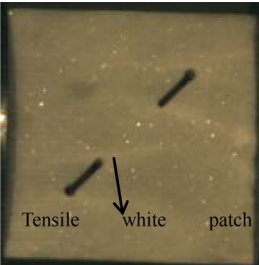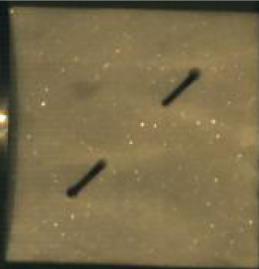
at the tips of the flaw at an angle to the flaws when the dynamic stress increases to 70.9 MPa (37.32% of the dynamic strength). Subsequently, a shear patch transforms into a tensile patch during the propagation process. Subsequently, the white patches widen, intensify, and lengthen to propagate to the edges of the specimen with some half X-shaped belts occurring as the dynamic stress approaches the peak value. When the stress starts to unload to 183.26 MPa (96.45%), shear cracks initiate at the tips of the flaw within the white patches.

4.2 Crack Types and Propagation

The crack propagation processes for the single-flawed specimens in the present tests are similar to results presented in our previous paper (Li et al. 2017b). Therefore, we only describe the crack propagation characteristics for the specimens with double flaws in this paper. The flaw tips closer to the edge of the specimen are defined as the outer tips and the other two tips are called the inner tips, as shown in Fig. 2.

Two types of cracks were observed in the present experiments, including shear and tensile cracks (the details of all tested specimens are described in Sect. 4.3), which are consistent with existing research results (Wong and Einstein 2009a, b, c; Yang et al. 2009; Park and Bobet 2010; Li et al. 2017b). However, different from the static compressive tests, it is observed that the shear cracks are generated earlier than the tensile cracks under dynamic loading, as shown in Table 4. When compressive waves with sufficient amplitude reach the flaw tips, shear cracks are generated, whereas tensile waves do not have enough time to form or to propagate to the interface between the incident bar and the specimen. This is the reason why the shear cracks initiate earlier than the tensile cracks (Li and Wong 2012). Due to the combined effects of the shear cracks and compressive waves, tensile cracks may initiate from the far field at the boundary of the specimen with the increase in the dynamic loading. In general, shear cracks dominate the crack propagation and ultimate failure of the rock materials.

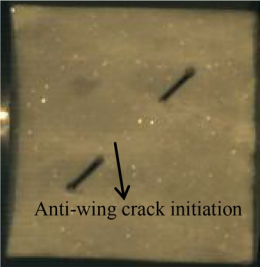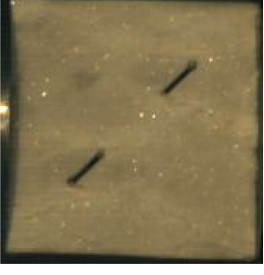**Table 3** Typical development of white patches under SHPB test (specimen M-2-45-45)

Cracking sequence	Stress (percentage of peak stress)/ MPa	Loading time/μs	Cracking sequence
	0	0	Start point of dynamic loading
	70.9 (37.32%)	62.5	Shear white patches firstly initiate at the tips of flaws at an angle with flaws
	133.34 (70.18%)	87.5	A shear patch transforms into a tensile patch during the propagation process
	162.14 (85.34%)	100.0	White patches expand and extend to be wider and intensified, then arrive at the edge of the specimen, finally form half X-shape belts
	183.26 (96.45%)	112.5	Shear cracks initiate at the tips of the flaw along the white patches trajectories

Loading direction: from the right to the left

Two types of shear cracks are generated in these tests, including coplanar or quasi-coplanar and oblique shear cracks (as shown in Fig. 8). The coplanar or quasi-coplanar shear cracks extend approximately along the plane of the flaw, whereas the oblique shear cracks initiate at an angle to the flaw plane. The shear crack initiation type depends

Table 4 Development of macroscopic cracks in specimen with double flaws under SHPB tests (specimen M-2-45-45)

Cracking sequence	Stress (percentage of peak stress)/ MPa	Loading time/μs	Cracking sequence
Shear crack initiation	183. 26(96.45%)	112.5	Shear cracks 1 and 2 initiate at the tip of the flaw corresponding to the white patch position. Tensile white patches propagate along the loading direction stably
Anti-wing crack initiation	177.50 (93.42%)	137.5	Shear cracks widen and lengthen along the white patch trajectories. Then shear crack 2 transforms into a wing crack along the loading direction, as a mixed crack defined in Sect. 4.3
	158.30 (83.32%)	150.0	All cracks expand and extend to wider and intensified belts full with rock powders
Tensile crack initiation	107.41 (56.53%)	175.0	Cracks arrive at the edge of the specimen to form half X shape belts

on the flaw angle α and ligament angle β to a large extent. When the flaw inclination angle is 30° and 45°, both coplanar and oblique shear cracks occur, except for M-2-45-75, which only had oblique shear cracks. For the rest of the specimens (the flaw inclination angles are 0°, 60°, 75°, and 90°), only oblique shear cracks are observed and they may be constrained by the cracks around the other flaw. The observed phenomena are different from that observed in the single-flaw marble specimens (Li et al. 2017b). This may indicate that the effect of the flaw number is much greater than the effect of the ligament angle on the crack generation types. The shear cracks initiate at the inner tips when α is smaller than 60° and β is smaller than 45°, whereas, for M-2-0-75 and M-2-90-30, they initiate from the outer tips. However, for other specimens, the shear cracks initiate at the inner and outer tips simultaneously. When α is constant and in the range of 0°–60°, the initiation positions change from the inner to the outer or inner-outer (most) tips as the ligament angle increases. When $\beta \leq 45°$, the initiation positions change from the inner to
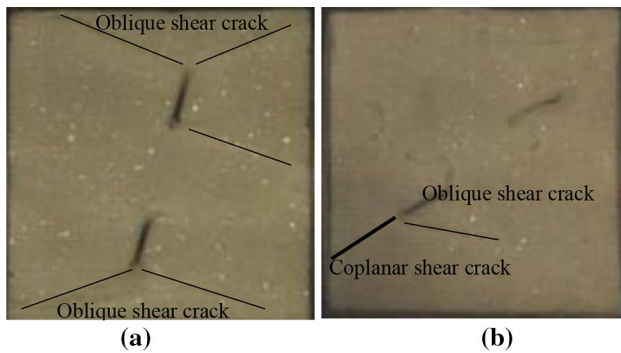
Fig. 8 Typical shear crack patterns of marble specimens under SHPB tests. **a** oblique shear cracks for specimen M-2-75-75; **b** coplanar shear cracks and oblique shear cracks for specimen M-2-30-45 (dynamic loading direction: from the right to the left part)
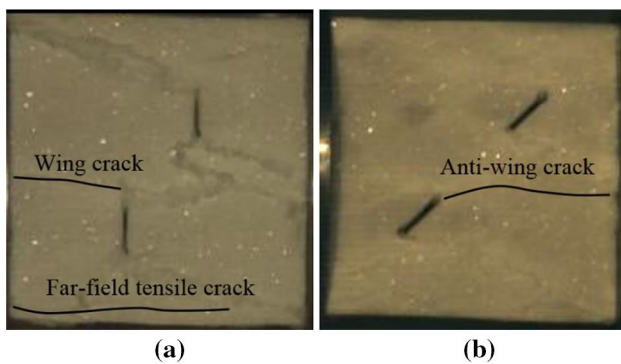

Fig. 9 Typical tensile crack patterns of marble specimens under SHPB tests. **a** wing tensile crack and far-field tensile crack for specimen M-2-90-45; **b** anti-wing crack for specimen M-2-45-45 (dynamic loading direction: from the right to the left part)

the inner-outer tips as the flaw inclination angle increases but the positions are all inner-outer tips if $\beta > 75°$.

Three types of tensile cracks were observed in the tests, including wing tensile cracks, anti-wing cracks, and far-field tensile cracks (as shown in Fig. 9). The far-field (secondary) tensile and anti-wing tensile cracks were observed for all specimens, but the wing cracks were mostly generated in specimens with flaw inclination angles equal to 0° and 90°. In addition, it appears that wing cracks are more likely to occur at a larger ligament angle.

Table 4 shows the macroscopic crack propagation process of a specimen with double flaws named M-2-45-45 in the SHPB test with a strain rate of 50.3 s^{-1}. When the compressive stress increases to 96.45% of the peak stress at the time of 112.5 µs, a macroscopic shear crack initiates at the tips of the flaw along the patch trajectory; subsequently, a shear crack transforms into a tensile crack along the loading direction to form a mixed crack, which is defined in Sect. 4.3. When the dynamic stress is unloaded in the post-peak stage,

more cracks generate and propagate along the trajectory of the white patches. Finally, all cracks rapidly develop and the dominant shear cracks expand and extend to cause the failure of the marble specimen.

4.3 Failure Modes of the Specimens with Double Flaws

The effects of the flaw inclination angle and ligament angle on the final failure mode are listed in Table 5. Li et al. (2017b) summarized the failure modes of single-flaw specimens under dynamic loading. For an intact specimen (M$_0$), a typical axial splitting tensile failure occurs. However, the failure modes of specimens with double flaws differ from those of the M$_0$ and single-flaw specimens.

Nine crack types were observed and are categorized based on their initiation and propagation mechanism for the specimens with double flaws under dynamic loadings. As shown in Fig. 10, four of the crack types are tensile cracks (Types I, II, III, and IV), four are shear cracks (Types IV, V, VI, and VIII), and the remaining one is a mixed shear-tensile crack (Type IX). Following are the details of the crack types:

Type I: For specimens with flaw inclination angles equal to 0° and 90°, wing and anti-wing cracks initiate at or near the internal tips of the flaw and then propagate along the loading direction independently; the crack coalescence does not occur between the two pre-existing flaws. Especially for an angle of 90°, this type of crack also dominates the failure of specimens with other shear cracks.

Type II: This type is similar to Type I. The cracks also initiate at or near the internal tips of the flaw and then propagate along the axial direction. The difference between Type I and Type II is the primary direction of crack initiation; for Type II, the primary crack initiation path is parallel to the dynamic loading, whereas, for Type I, the path is first curvilinear and then propagates along the axial stress.

Type III: Anti-wing cracks initiate from the internal tips of the two pre-existing flaws and then develop along the direction of the axial stress without the occurrence of crack coalescence in the ligament region.

Type IV: When the stress reaches the post-peak stage, the far-field tensile cracks always initiate at the interface between the bar and specimen and at a distance away from the internal tips of the flaws. They are usually not the dominant cracks that lead to the collapse of the specimens with double flaws.

Type V: The shear cracks initiate near the internal tips or the center position of two pre-existing flaws. With increasing dynamic loading, the cracks widen and eventually expand into shear belts covered with pulverized rock powder. Finally, the crack coalescence of the shear cracks occurs between the two flaws. It is evident from Table 5 that

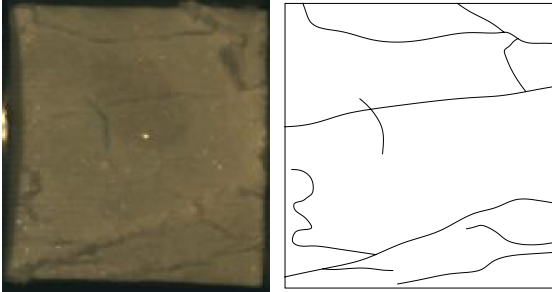**Table 5** Failure modes of intact and double-flawed marble specimens under SHPB tests
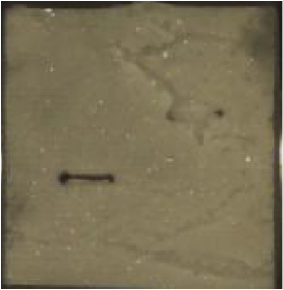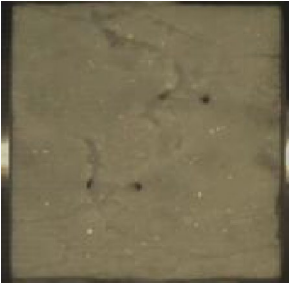
Specimen	Ligament angle / °		
no.	30	45	75

Table 5 (continued)

M-2-45

M-2-60

M-2-75
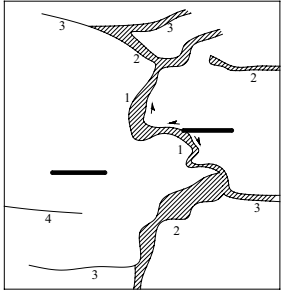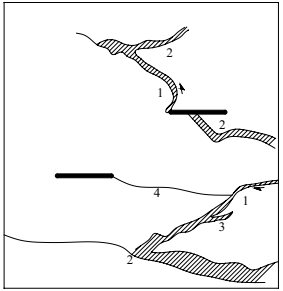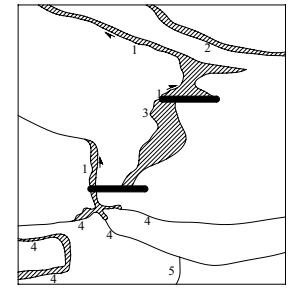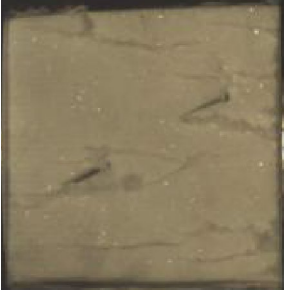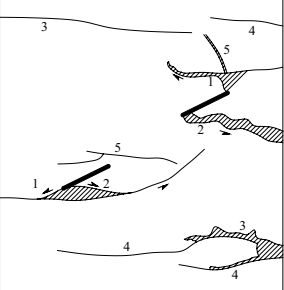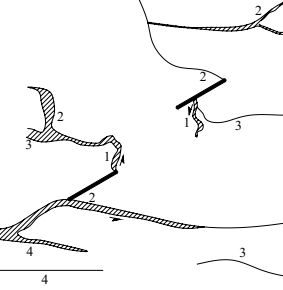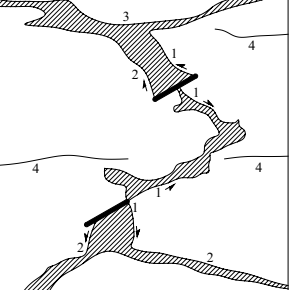
Table 5 (continued)

M-2-90

Numbers represent the sequence of crack initiation

this type of crack generates easily when the flaw inclination angle is equal to or larger than 45°.

Type VI: Oblique shear cracks initiate at or near the flaw tips of specimens with double flaws but propagate to the boundary of the specimen and always evolve into wider shear belts covered with pulverized rock debris. There is no crack coalescence between the two pre-existing flaws. This type of crack occurs in specimens with relatively large flaw inclination angles and ligament angles, i.e., M-2-90-75.

Type VII: Oblique shear cracks initiate at or near the tips of two pre-existing flaws but propagate parallel to the dynamic loading independently and without coalescence, usually leading to a greater width filled with rock powder, i.e., M-2-75-75.

Type VIII: Secondary shear cracks always initiate at the edges of the specimen at a distance away from the pre-existing flaws; these cracks do not dominate the crack propagation and failure process.

Type IX: Mixed shear-tensile cracks first initiate mostly as shear cracks then transform into tensile cracks and propagate along the loading direction, while a few initial tensile cracks transform into shear cracks and propagate at an acute angle to the flaw direction in a stable manner.

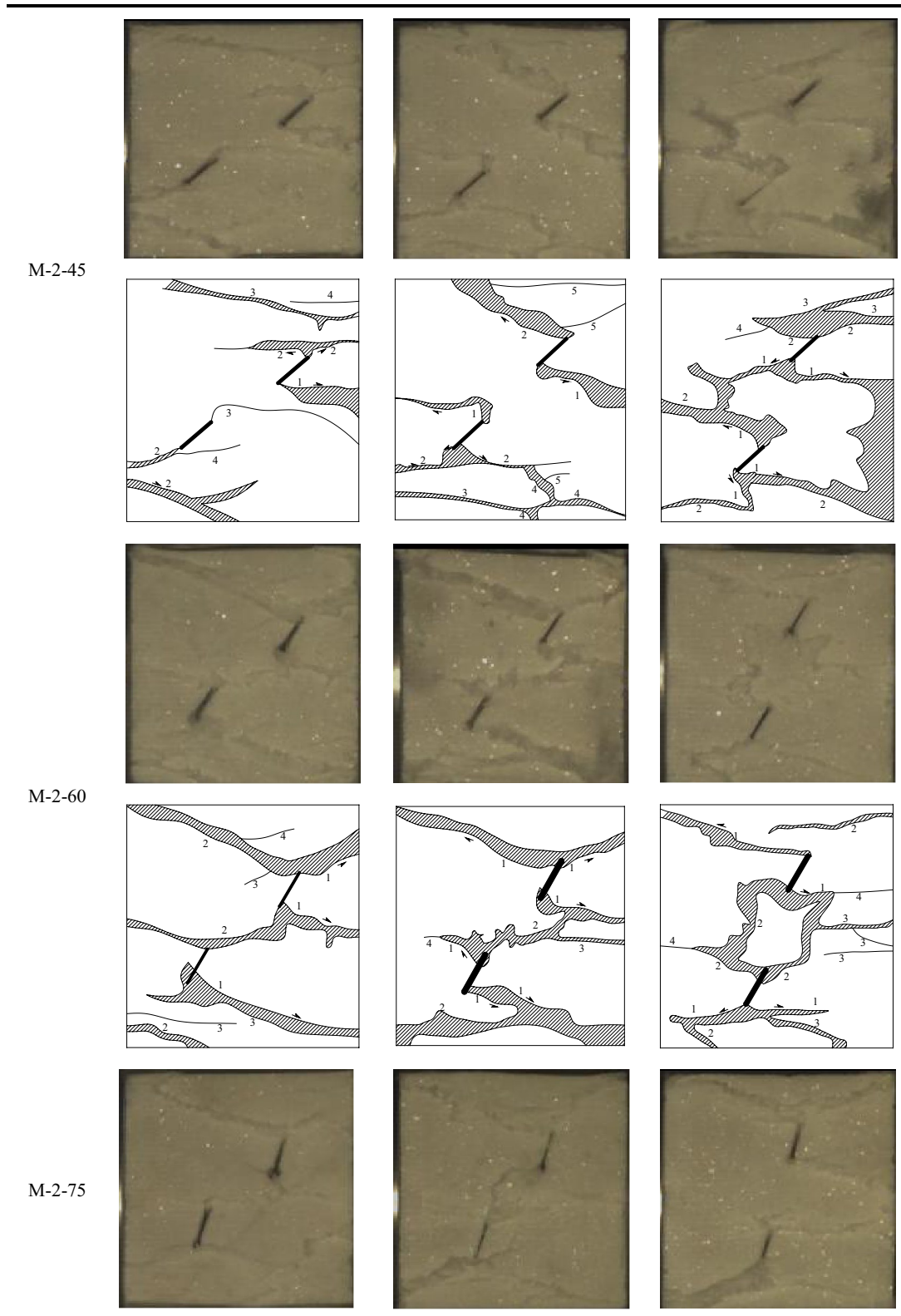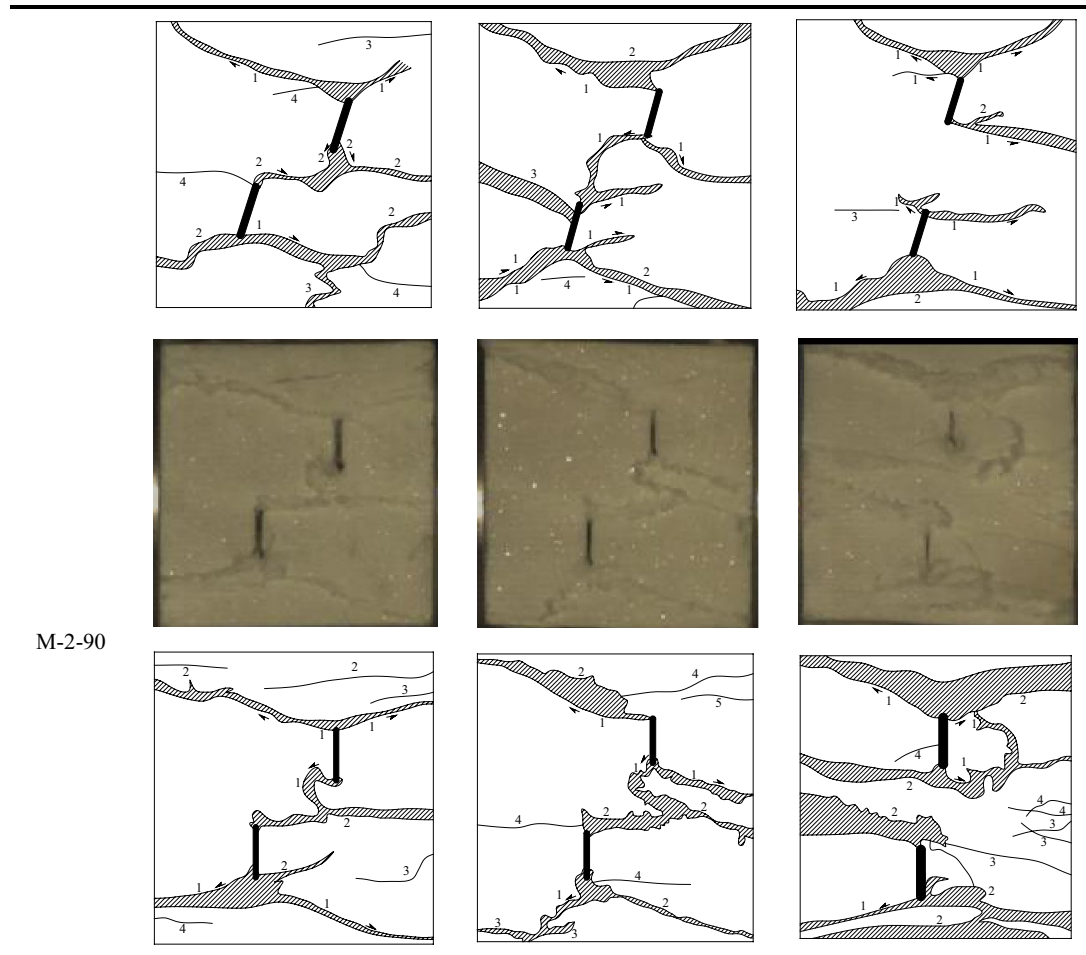Table 6 summarizes the crack types of the intact marble specimens and specimens with double flaws in response to the applied dynamic loading. The failure mode of the marble specimen with double flaws has a close relationship to the geometry of the pre-existing flaws with regard to α and β. Moreover, according to the above analysis, the failure of the marble specimen with double flaws includes both shear and tensile cracks. Shear cracks first initiate at the tips of the flaw and finally form X- or half X-shaped white belts filled with rock powders that dominate the crack propagation and ultimate cause the failure of almost all flawed specimens.

4.4 Crack coalescence

With the aid of the high-speed camera, we observed and analyzed the crack coalescence from the inner and outer tips of the pre-existing flaws in the marble specimens. It is found
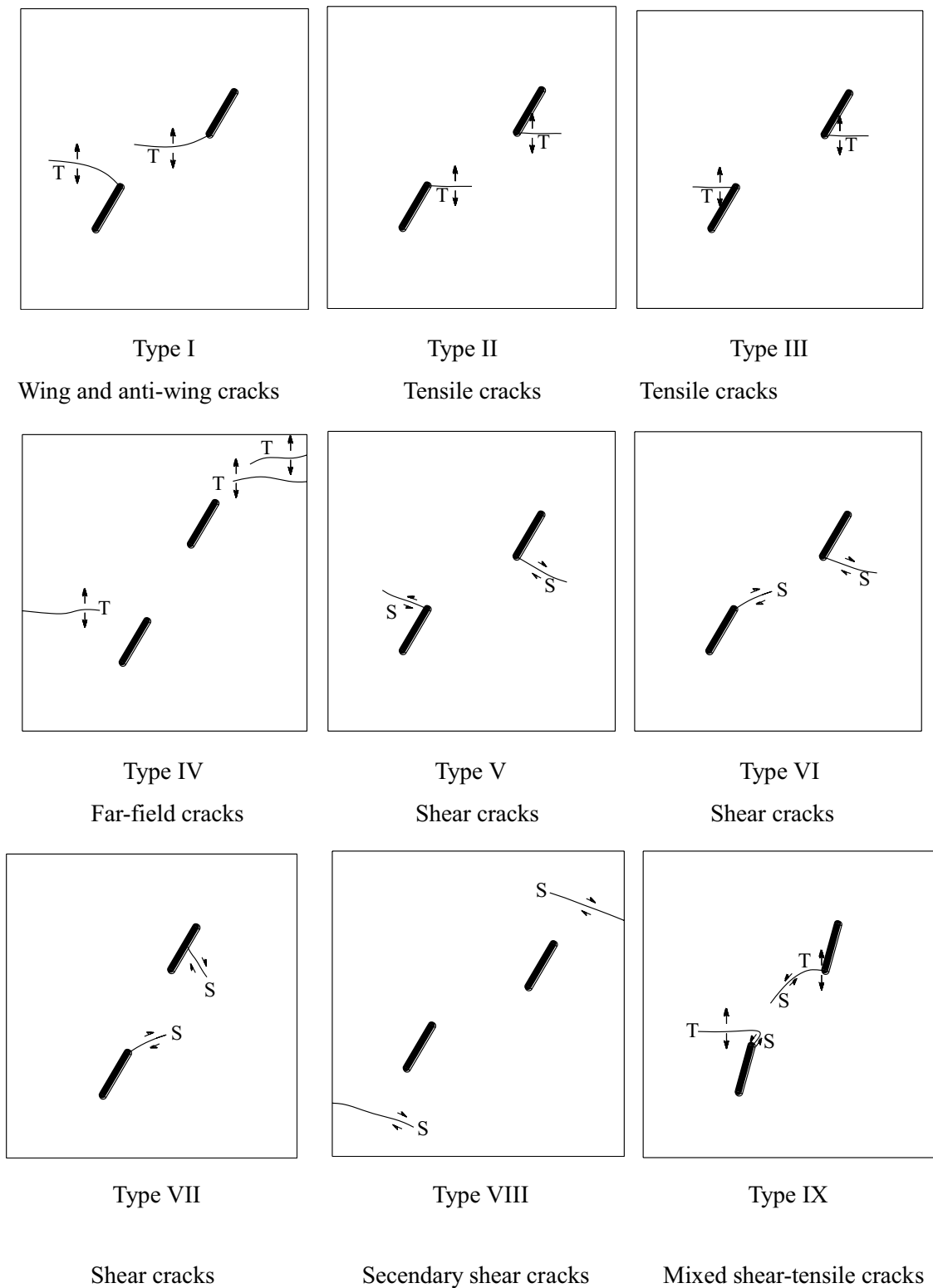
Fig. 10 Various typical crack types identified in double flawed specimens in the present study. *T* tensile crack, *S* shear crack (dynamic loading direction: from the right to the left part)

Table 6 Crack types of intact and double flawed marble specimens under SHPB tests

Specimen no.	Type I	Type II	Type III	Type IV	Type V	Type VI	Type VII	Type VIII	Type IX	Remark
M_0									$\checkmark^1$	
M-2-0-30						$\checkmark^1$			$\checkmark$	
M-2-0-45	$\checkmark$				$\checkmark^1$			$\checkmark$	$\checkmark^1$	
M-2-0-75	$\checkmark$			$\checkmark$			$\checkmark^1$	$\checkmark$		
M-2-30-30						$\checkmark^1$		$\checkmark$	$\checkmark$	
M-2-30-45	$\checkmark^1$				$\checkmark^1$	$\checkmark$			$\checkmark$	
M-2-30-75				$\checkmark^1$	$\checkmark$			$\checkmark$		
M-2-45-30	$\checkmark$				$\checkmark^1$			$\checkmark$		
M-2-45-45		$\checkmark$			$\checkmark^1$		$\checkmark$		$\checkmark$	
M-2-45-75						$\checkmark^1$	$\checkmark$	$\checkmark$	$\checkmark$	
M-2-60-30				$\checkmark^1$	$\checkmark$			$\checkmark$	$\checkmark$	
M-2-60-45				$\checkmark^1$	$\checkmark$	$\checkmark$		$\checkmark$		
M-2-60-75					$\checkmark$	$\checkmark^1$	$\checkmark$	$\checkmark$	$\checkmark$	
M-2-75-30				$\checkmark^1$	$\checkmark$		$\checkmark$		$\checkmark$	
M-2-75-45				$\checkmark^1$	$\checkmark^1$	$\checkmark$	$\checkmark$		$\checkmark$	
M-2-75-75					$\checkmark$	$\checkmark^1$	$\checkmark$		$\checkmark$	
M-2-90-30	$\checkmark^1$	$\checkmark$	$\checkmark$				$\checkmark^1$		$\checkmark$	
M-2-90-45	$\checkmark^1$	$\checkmark$			$\checkmark^1$				$\checkmark$	
M-2-90-75	$\checkmark$	$\checkmark^1$	$\checkmark$				$\checkmark$		$\checkmark$	

$\checkmark^1$ Indicates that the crack is the first crack to initiate

that the ultimate failure modes are dependent on the flaw inclination angle α and the ligament angle β. The types of crack coalescence modes in our tests are the same as those reported in previous studies for static loadings, i.e., tensile mode, shear mode, and mixed shear-tensile mode. Figure 10 summarizes the nine different crack patterns observed in our tests. There are three modes of crack coalescence: (1) Wing/tensile crack coalescence (Fig. 10 I-III); (2) shear crack coalescence (Fig. 10 V-VII); (3) mixed shear-tensile crack coalescence (Fig. 10 IX).

The wing and tensile crack coalescence outside the ligament area consists of three types: I-III. As shown in Fig. 10, the type-I coalescence refers to two wing cracks propagating along the same direction and this mostly occurs at $\alpha = 90°$ or a lower flaw inclination angle ($\leq 45°$) with a ligament angle smaller than 45°. We can see that the wing and tensile crack coalescence at $\alpha = 90°$ is a combination of the three types. For type II and type III, the tensile cracks appear at the inner tips of the two pre-existing flaws and then propagate along the loading direction; these cracks are observed mostly for $\alpha = 90°$. We can see that the wing and tensile crack coalescence at $\alpha = 90°$ is a combination of these three types.

The shear crack coalescence contains three types: V-VII. As shown in Fig. 10, the only difference between the type V

and type III is the nature of the crack. A type VI crack is produced at the upper flaw and has a smaller deflection angle, whereas the crack produced at the lower flaw is greatly deflected upwards and is connected to the upper crack at the end of the rock bridge. But for type VII, the two cracks have approximately the same degree of deflection and finally coalesce in the bridge area.

The mixed shear-tensile crack coalescence is plotted in Fig. 10 IX. It can be further divided into two types: (1) the tensile cracks initiate from the inner tips but develop into shear cracks; (2) this is the opposite in that the shear cracks initiate from the inner tips but develop into tensile cracks. This type is probably caused by a slight difference in the frictional coefficient between the upper and lower flaw surfaces (Wong and Chau 1998).

4.5 Comparison of Cracking Behavior under Dynamic and Quasi-static Loadings

In static tests, the ultimate failure of flawed specimens is caused by the main cracks initiated at the flaw tips. However, under dynamic loading, the initial positions of the dominant cracks are not only at the flaw tips as mentioned above but also in the area around the flaw tips. In addition, there are more secondary cracks observed
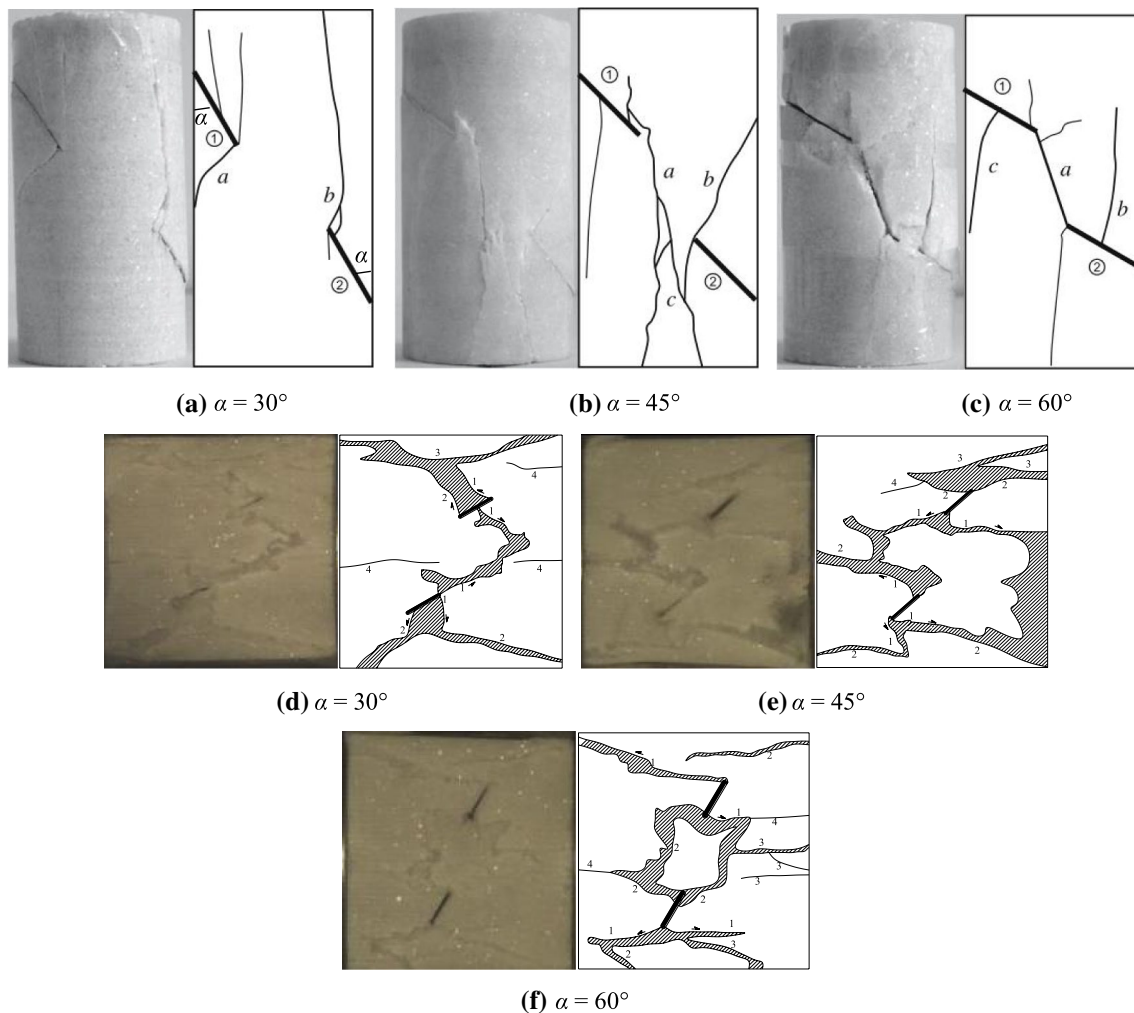
(a) $\alpha = 30°$ **(b)** $\alpha = 45°$ **(c)** $\alpha = 60°$

(d) $\alpha = 30°$ **(e)** $\alpha = 45°$

(f) $\alpha = 60°$

Fig. 11 Failure modes of marble specimens containing double flaws with different flaw angles under **a–c** uniaxial compression (Yang et al. 2009); **d–f** dynamic loading ($\beta = 75°$)

under dynamic loading than under static failure and these cracks finally results in more small fragments, as shown in Fig. 11.

Under static loading, the tensile cracks always initiate simultaneously with shear cracks when there are two flaws in marble specimens (Yang et al. 2009). Shear cracks are observed in addition to tensile cracks in specimens with double flaws for $\alpha = 45°$, which shows that a moderate flaw angle is more likely to result in a mixed failure of the specimen, as shown in Fig. 11b. In dynamic tests, the shear cracks are mostly generated earlier than the tensile cracks. The flaw angle has a complex effect on the crack propagation and coalescence. Both coplanar and oblique shear cracks are observed for α between 30° and 45° but only oblique shear cracks occur for α equal to 60°. Wing or anti-wing cracks are easier to initiate when α is larger than 30°, as shown in Fig. 11d–f. The failure modes of the tested specimens consisted of a mixture of several cracks under quasi-static and dynamic loadings. However, the shear cracks are the dominant crack types under dynamic loadings, whereas the tensile cracks are the dominant crack types under quasi-static loadings (Zou et al. 2016).

Table 7 Energy properties of intact and flawed marble specimens under SHPB tests

Specimen no.	Incident energy/J	Reflected energy/J	Transmitted energy/J	Absorbed energy/J	R/%	Remark
M_0	179.23	37.04	82.81	59.38	33.13	Intact specimen
M-1-0	251.34	64.58	102.50	84.26	33.53	Flaw angle
M-1-30	192.79	41.23	67.47	84.09	43.62	
M-1-45	166.98	32.54	58.76	75.68	45.32	
M-1-60	189.77	39.65	67.09	83.03	43.79	
M-1-75	197.28	40.22	65.84	91.22	46.24	
M-1-90	188.30	40.13	57.83	90.34	47.99	
M-2-0-30	245.48	72.16	98.08	75.24	30.65	Flaw angle and Ligament angle
M-2-0-45	244.29	125.48	56.15	62.66	25.65	
M-2-0-75	272.83	107.23	74.34	91.26	33.45	
M-2-30-30	227.51	53.36	74.25	99.90	43.91	
M-2-30-45	224.16	54.33	70.08	99.75	44.5	
M-2-30-75	206.74	41.98	56.76	108.00	52.24	
M-2-45-30	229.15	77.91	56.99	94.25	41.13	
M-2-45-45	244.72	73.09	74.28	97.35	39.78	
M-2-45-75	249.82	122.02	37.84	89.96	36.01	
M-2-60-30	228.53	133.16	37.53	57.84	25.31	
M-2-60-45	251.72	122.41	40.88	88.43	35.13	
M-2-60-75	236.96	122.52	34.49	79.95	33.74	
M-2-75-30	285.99	211.24	27.79	46.96	16.42	
M-2-75-45	273.16	161.53	30.01	81.62	29.88	
M-2-75-75	272.67	171.94	28.01	72.72	26.67	
M-2-90-30	263.64	192.10	27.09	44.45	16.86	
M-2-90-45	287.88	181.04	39.88	66.96	23.26	
M-2-90-75	276.15	200.33	18.27	57.55	20.84	

5 Energy Evolution

5.1 Energy Properties

Rock failure depends on crack propagation and coalescence and is actually a process of energy dissipation. Therefore, it is of practical significance and to ensure the safety of many underground structures to analyze the law of energy consumption. Energy absorption is an essential feature of the crack propagation and failure process in rock materials and is directly related to the number and surface area of new cracks in rocks. Using the one-dimensional stress wave theory and the results from the SHPB tests, the incident energy E_I, the reflected energy E_R, and the transmitted energy E_T in the rock failure process can be calculated (Li 2014):

$$E_I = \frac{A_e}{\rho_e C_e} \int_0^\tau \sigma_I^2(t)dt \tag{4}$$

$$E_R = \frac{A_e}{\rho_e C_e} \int_0^\tau \sigma_R^2(t)dt \tag{5}$$

$$E_T = \frac{A_e}{\rho_e C_e} \int_0^\tau \sigma_T^2(t)dt, \tag{6}$$

where $\sigma_I(t)$, $\sigma_R(t)$, and $\sigma_t(t)$ are the incident, reflected and transmitted stress at time t respectively and $\rho_e C_e$ is the wave impedance of the bars.

The incident, reflected, and absorbed energy for the specimens with pre-existing flaws with different quantities, inclination angles, and ligament angles under dynamic loading are listed in Table 7, where R is the ratio of the absorbed energy to the incident energy. The absorbed energy is higher for the single-flaw specimens than the intact specimen. However, the absorbed energy of the single-flaw specimens changes little when α increases from 0° to 90°. In addition, most of the remaining energy is dissipated as transmitted energy to the transmitted bar. This phenomenon indicates that α may have a limited effect on the energy absorption of the specimens with a single pre-existing flaw during dynamic impact loading. The absorbed energy is higher for the specimens with double flaws than the intact specimen, except for the specimens with β equal to 30° and α larger
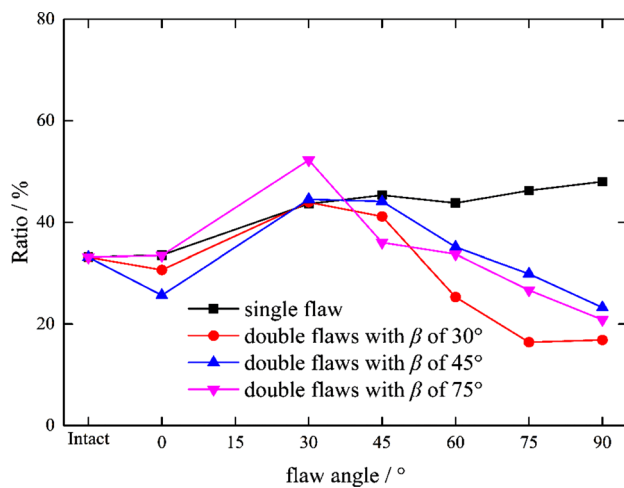
Fig. 12 Influence of flaw number, flaw angle and ligament angle on the ratio of absorbed to incident energy of flawed specimens under SHPB tests

than 60°. The absorbed energy of the specimens with double flaws first increases as α increases from 0° to 30° and then gradually decreases as α increases to 90°. This indicates that α has a significant influence on the energy absorption of the specimens containing double pre-existing flaws. Moreover, there may be a critical α (approximately 30°), below which the absorbed energy increases with α, whereas the absorbed energy decreases with α above this angle. In addition, it is found that β also affects the energy absorption for the specimens with the same α. When α is smaller than 45°, the specimens with β equal to 75° absorb more energy than those with β equal to 30° and 45°. When α is larger than 45°, the specimens with β equal to 45° and 30° absorb the most and least energy, respectively. Most of the remaining energy is dissipated as transmitted energy to the transmitted bar for $\alpha = 30°$, whereas it is dissipated as reflected energy for the other specimens, especially when α reaches 45°.

5.2 Ratio of Absorbed Energy to Incident Energy

The influence of the flaw parameters on the propagation of the stress waves in the flawed rock has been investigated for decades, including parameters such as flaw numbers (Li et al. 2010, 2012), flaw closure (Zhao and Cai 2003; Li and Ma 2009), microscopic discontinuities (Fan et al. 2012), and water content (Li and Ma 2009). The ratio of absorbed energy to incident energy characterizes the effective energy utilization for the fragmentation of rocks when stress waves propagate across rock masses. It is an important parameter for rock excavations, especially in deep hard rock engineering.

The ratios of the absorbed energy to the incident energy of the specimens with different flaw angles and ligament

inclination angles are plotted in Fig. 12. The ratio of the flawed specimens is higher for the single-flaw specimens than for the intact specimen. R gradually increases from 33.53 to 47.99% as α changing from 0° to 90°. This indicates that an increase in α may increase the energy absorption of the specimens with a single pre-existing flaw under dynamic compression.

For the specimens with the double flaws, the energy absorption ratio of the flawed specimens exhibits more complex variability than that of the intact and single-flaw specimens. The energy absorption ratio first increases when the flaw inclination angle ranges from 0° to 30° and then decreases with the increase in the flaw angle. The maximum value occurs at a flaw angle of $\alpha = 30°$. The ligament angle also has some effect on the changes in the energy absorption ratio. For the marble specimens with the double flaws and $\alpha > 30°$, there is a critical ligament angle at about 45°, at which the energy absorption is at a maximum value and it may be useful for the rock fragments under impact loading.

In general, the energy absorption ratio is in most cases higher for the single-flaw specimens than the specimens with double flaws, except for $\alpha = 30°$, indicating that the energy absorption may not be affected by the number of flaws. The energy absorption ratio is usually highest for the specimens with a single flaw. Since the dynamic strength is much lower for the double-flaw specimen than the single-flaw specimen, there is no need to absorb more energy to fracture the specimen with double flaws.

6 Conclusions

Rectangular prismatic flawed marble materials are used to investigate the dynamic mechanical properties, crack propagation, and energy distribution of specimens under impact tests. The conclusions are summarized as follows:

1. Pre-existing flaws change the shape of the complete dynamic stress–strain curves and the flaw geometry affects the dynamic strength and deformation properties of the marble specimens. The dynamic strength is greatly weakened by a larger number of flaws, a larger inclination angle α, and an appropriate ligament angle β. The dynamic strain exhibits more complex change characteristics as a result of different flaws. The flaw inclination angle has the same effect on the strength but a different effect on the strain under static loadings, whereas the ligament angle has little influence on the static mechanical and deformation behaviors.

2. Prior to the appearance of macroscopic cracks, shear white patches initiate at the tips of the flaws when α is less than 60° and β is less than 45°. When α and β are increasing, the shear white patches may initiate near

the center of the flaws. The shear white patches usually become wider and form intensified belts with an X or half X shape, but the tensile white patches have a linear shape and they increase with the increase in the dynamic loading.

3. The shear cracks usually generate earlier than the tensile cracks and dominate the crack propagation process. The ultimate failure of the marble materials is characterized by X or half X shear belts that are filled with rock powder. The tensile cracks usually initiate from the far field at the end of the specimen and propagate in a stable manner without the presence of much rock powder. However, the tensile cracks dominate the cracking process in the static tests.

4. Nine different crack coalescence types are identified in the crack initiation and propagation mechanism under dynamic loading in the present research. The failure mode of the marble specimen with double flaws has a close relationship to the geometry of the flaw with regard to α and β. A mixture of the nine crack types is observed, including shear and tensile cracks.

5. The absorbed energy of the flawed specimens is usually larger than that of the intact specimen, except for specimens with double flaws and $\alpha > 60°$ and $\beta = 30°$. The ratio (absorbed energy to incident energy) is higher for the single-flaw specimens than the intact specimen. However, the ratio is higher for specimens with double flaws than for intact specimens only when the flaw inclination angle is in the range of $30°$–$60°$ (except for M-2-60-30). The energy properties are more complex for the flawed specimens and are distinctly influenced by the flaw geometries including the flaw number, flaw angle, and ligament angle.

References

Bobet A, Einstein HH (1998) Fracture coalescence in rock-type materials under uniaxial and biaxial compression. Int J Rock Mech Min Sci 35(7):863–888

Dai F, Huang S, Xia K, Tan Z (2010) Some fundamental issues in dynamic compression and tension tests of rocks using split Hopkinson pressure bar. Rock Mech Rock Eng 43(6):657–666

Fan LF, Ma GW, Wong LNY (2012) Effective viscoelastic behaviour of rock mass with double-scale discontinuities. Geophys J Int 191(1):147–154

Fan LF, Yi XW, Ma GW (2013) Numerical manifold method (NMM) simulation of stress wave propagation through fractured rock mass. Int J Appl Mech 5(02):249–268

Fang Z, Harrison JP (2002) Development of a local degradation approach to the modelling of brittle fracture in heterogeneous rocks. Int J Rock Mech Min Sci 39:443–457

Inglis CE (1913) Stresses in a plate due to the presence of cracks and sharp corners. Proc Inst Nav Arch 55(1):219–230

Jeong J, Adib H, Pluvinage G (2005) Proposal of new damage model for thermal shock based on dynamic fracture on the brittle materials. J Non-Cryst Solids 351(24):2065–2075

Jiang C, Zhao GF, Zhu J, Zhao YX, Shen L (2016) Investigation of dynamic crack coalescence using a gypsum-like 3D printing material. Rock Mech Rock Eng 49(10):3983–3998

Lee H, Jeon S (2011) An experimental and numerical study of fracture coalescence in pre-cracked specimens under uniaxial compression. Int J Solids Struct 48(6):979–999

Li X (2014) Rock dynamic: fundamentals and applications. Science Press, Beijing

Li JC, Ma GW (2009) Experimental study of stress wave propagation across a filled rock joint. Int J Rock Mech Min Sci 46(3):471–478

Li HB, Wong LNY (2012) Influence of flaw inclination angle and loading condition on crack initiation and propagation. Int J Solids Struct 49(18):2482–2499

Li X, Lok TS, Zhao J (2005a) Dynamic characteristics of granite subjected to intermediate loading rate. Rock Mech Rock Eng 38(1):21–39

Li YP, Chen LZ, Wang YH (2005b) Experimental research on pre-cracked marble under compression. Int J Solids Struct 42(9–10):2505–2516

Li X, Zhou Z, Hong L, Yin T (2009) Large diameter SHPB tests with a special shaped striker. ISRM News J 12:76–79

Li JC, Ma GW, Zhao J (2010) An equivalent viscoelastic model for rock mass with parallel joints. J Geophys Res-Solid Earth 115(B3)

Li JC, Li HB, Ma GW, Zhao J (2012) A time-domain recursive method to analyse transient wave propagation across rock joints. Geophys J Int 188(2):631–644

Li D, Cheng T, Zhou T, Li X (2015) Experimental study of the dynamic strength and fracturing characteristics of marble specimens with a single hole under impact loading. Chin J Rock Mech Eng 34(2):249–260 **(in Chinese)**

Li X, Wu Q, Tao M, Weng L, Dong L, Zou Y (2016) Dynamic Brazilian splitting test of ring-shaped specimens with different hole diameters. Rock Mech Rock Eng 49(10):4143–4151

Li D, Zhu Q, Zhou Z, Li X, Ranjith PG (2017a) Fracture analysis of marble specimens with a hole under uniaxial compression by digital image correlation. Eng Fract Mech 183:109–124

Li X, Zhou T, Li D (2017b) Dynamic strength and fracturing behavior of single-flawed prismatic marble specimens under impact loading with a split-Hopkinson pressure bar. Rock Mech Rock Eng 50(1):1–16

Li M, Zhu Z, Liu R, Liu B, Zhou L, Dong Yu (2018) Study of the effect of empty holes on propagating cracks under blasting loads. Int J Rock Mech Min Sci 103:186–194

Liang ZZ, Xing H, Wang SY, Williams DJ, Tang CA (2012) A three-dimensional numerical investigation of the fracture of rock specimens containing a pre-existing surface flaw. Comput Geotech 45(45):19–33

Luo L, Li X, Tao M, Dong L (2017) Mechanical behavior of rock-shotcrete interface under static and dynamic tensile loads. Tunn Undergr Space Technol 65:215–224

Morgan SP, Johnson CA, Einstein HH (2013) Cracking processes in Barre granite: fracture process zones and crack coalescence. Int J Frac 180(2):177–204

Park CH, Bobet A (2010) Crack initiation, propagation and coalescence from frictional flaws in uniaxial compression. Eng Fract Mech 77(14):2727–2748

Qiu J, Li D, Li X (2017) Dynamic failure of a phyllite with a low degree of metamorphism under impact Brazilian test. Int J Rock Mech Min Sci 94:10–17

Shen B, Stephansson O, Einstein HH, Ghahreman B (1995) Coalescence of fractures under shear stresses in experiments. J Geophys Re-Solid Earth 100(B4):5975–5990

Wang SY, Sloan SW, Tang CA (2014) Three-dimensional numerical investigations of the failure mechanism of a rock disc with a central or eccentric hole. Rock Mech Rock Eng 47(6):2117–2137

Wong RHC, Chau KT (1998) Crack coalescence in a rock-like material containing two cracks. Int J Rock Mech Min Sci 35(2):147–164

Wong LNY, Einstein HH (2009a) Crack coalescence in molded gypsum and carrara marble: Part 1. Macroscopic observations and interpretation. Rock Mech Rock Eng 42(3):475–511

Wong LNY, Einstein HH (2009b) Crack coalescence in molded gypsum and carrara marble: part 2—microscopic observations and interpretation. Rock Mech Rock Eng 42(3):513–545

Wong LNY, Einstein HH (2009c) Systematic evaluation of cracking behavior in specimens containing single flaws under uniaxial compression. Int J Rock Mech Min Sci 46(2):239–249

Wu ZJ, Wong LNY, Fan LF (2013) Study of dynamic fracture problems in viscoelastic sedimentary rocks using the numerical manifold method. Rock Mech Rock Eng 46(6):1415–1457

Xia K, Yao W (2015) Dynamic rock tests using split Hopkinson (Kolsky) bar system—a review. J Rock Mech Geotech 7(1):27–59

Yang SQ, Dai YH, Han LJ, Jin ZQ (2009) Experimental study on mechanical behavior of brittle marble samples containing different flaws under uniaxial compression. Eng Fract Mech 76(12):1833–1845

Yang SQ, Huang YH, Tian WL, Zhu JB (2017) Erratum to: an experimental investigation on strength, deformation and crack evolution behavior of sandstone containing two oval flaws under uniaxial compression. Eng Geol 217:35–48

Yin P, Wong RHC, Chau KT (2014) Coalescence of two parallel pre-existing surface cracks in granite. Int J Rock Mech Min Sci 68(6):66–84

Zhang QB, Zhao J (2013) Determination of mechanical properties and full-field strain measurements of rock material under dynamic loads. Int J Rock Mech Min Sci 60(8):423–439

Zhang QB, Zhao J (2014) A review of dynamic experimental techniques and mechanical behaviour of rock materials. Rock Mech Rock Eng 47(4):1411–1478

Zhao J, Cai JG (2003) Transmission of elastic P-waves across single fractures with a nonlinear normal deformational behavior. Chin J Rock Mech Eng 34(1):3–22

Zhou Y, Xia K, Li X, Li H, Ma G, Zhao J, Zhou Z, Dai F (2011) Suggested methods for determining the dynamic strength parameters and mode-I fracture toughness of rock materials. Int J Rock Mech Min Sci 49(1):105–112

Zhou L, Zhu Z, Wang M, Ying P, Dong Y (2018) Dynamic propagation behavior of cracks emanating from tunnel edges under impact loads. Soil Dyn Earthq Eng 105:119–126

Zou C, Wong LNY (2014) Experimental studies on cracking processes and failure in marble under dynamic loading. Eng Geol 173(5):19–31

Zou C, Wong LNY, Jin JL, Gan BS (2016) Different mechanical and cracking behaviors of single-flawed brittle gypsum specimens under dynamic and quasi-static loadings. Eng Geol 201(4):71–84